

*Chapter 3***FOCUSING THROUGH DYNAMIC TISSUE WITH
MILLISECOND DIGITAL OPTICAL PHASE CONJUGATION**

This chapter is adapted from the manuscript Wang, D., Zhou, E.H.*, Brake, J., Ruan, H., Jang, M. & Yang, C. "Focusing through dynamic tissue with millisecond digital optical phase conjugation". *Optica* 2, 728 (2015). The contributions of authors are as follows: HR, MJ and CY conceived the initial idea. EHZ and DW developed the idea and experimental scheme. The experiments were designed and performed by EHZ and DW. The data analyses were performed by DW, EHZ, HR, and CY. * denotes equal contribution to the work.*

Digital optical phase conjugation (DOPC) is a new technique employed in wavefront shaping and phase conjugation for focusing light through or within scattering media such as biological tissues. DOPC is particularly attractive as it intrinsically achieves a high fluence reflectivity in comparison to non-linear optical approaches. However, the slow refresh rate of liquid crystal spatial light modulators and limitations imposed by computer data transfer speeds have thus far made it difficult for DOPC to achieve a playback latency shorter than ~ 200 ms and therefore prevented DOPC from being practically applied to thick living samples. In this paper, we report a novel DOPC system that is capable of 5.3 ms playback latency. This speed improvement of almost two orders of magnitude is achieved by using a DMD (digital micromirror device), field programmable gate array (FPGA) processing, and a single-shot binary phase retrieval technique. With this system, we are able to focus through 2.3 mm living mouse skin with blood flowing through it (decorrelation time ~ 30 ms) and demonstrate that the focus can be maintained indefinitely—an important technological milestone that has never been previously reported.

3.1 Introduction

Focusing light through tissues has long been a challenge for biomedical optics. The turbid nature of tissues strongly scatters light and hinders the formation of a sharp focus. Recently, research in the field of wavefront shaping has shown that by correcting the wavefront incident on scattering media, focus can be constructed at an arbitrary location behind the sample [1, 2]. Different strategies have been developed to realize this process, including iterative wavefront optimization [1, 3–

5], transmission matrix measurement [6–8], and optical phase conjugation (OPC) [9–11]. Among these, OPC implements the corrected wavefront by recording the scattered light field globally and then playing back the conjugate light field by a phase conjugate mirror (PCM) without time-consuming iterations. Since the process of elastic light scattering is time symmetric, by playing a conjugate version of the scattered wavefront back through the scattering medium, the conjugate input wavefront can be recovered.

By employing OPC, a number of novel techniques for focusing light through or within a scattering medium have recently been developed. These include TRUE (Time-Reversed Ultrasonically Encoded Light) [12, 13], TROVE (Time Reversal of Variance-Encoded light) [14], TRACK (Time Reversal by Analysis of Changing wavefronts from Kinetic targets) [15], and TRAP (Time-Reversed Adapted-Perturbation) focusing [16]. These methods have the potential to improve or enable biomedical applications such as deep tissue imaging, photodynamic therapy, and noninvasive cytometry.

There are two major advantages of OPC compared to other wavefront shaping techniques. First, it is able to arrive at the correct wavefront solution without iteration. Second, the number of controllable optical modes in the playback wavefront can be very high; $\sim 5 \times 10^5$ modes or more. Optical phase conjugation methods can be categorized into two primary groups. Non-linear OPC methods [12, 17, 18] employ non-linear crystals to store the scattered field and propagate the phase conjugate field. In contrast, the digital optical phase conjugation (DOPC) method [13–16] uses an electronic camera in an interferometric setup to capture the optical wavefront information and subsequently produce a suitable OPC field by using that information to pattern a spatial light modulator.

The DOPC method has several intrinsic advantages over non-linear OPC methods. First, whereas non-linear crystals are strongly dependent on wavelength, DOPC can freely work with a broad range of wavelengths. Second, DOPC provides the flexibility to render wavefront playback beyond a single OPC field. In fact, TROVE, TRACK, and TRAP all exploit this unique capability of DOPC to render complex and nuanced wavefronts. In the case of TRACK and TRAP for example, the rendered wavefront is actually a differential DOPC wavefront. Third, and perhaps most importantly, the DOPC method has the intrinsic ability to achieve a fluence reflectivity greater than unity. Here we define fluence reflectivity as the ratio between the total amount of light that one can play back on the conjugate wavefront to the total

amount of scattered light required to determine the conjugate wavefront in the first place. While nonlinear OPC methods can in principle provide gain enhancement by temporally squeezing the playback photon packet [19], a practical and useful approach to deliver large amounts of energy over an extended period of time has not been demonstrated.

Currently, the DOPC method does have a significant disadvantage versus nonlinear OPC methods – response speed. Recently, nonlinear methods with system response latencies on the order of milliseconds have been reported [20, 21]. In contrast, DOPC systems reported thus far have response times on the order of hundreds of milliseconds or more [22]. This slow response is due to the use of slow liquid crystal spatial light modulators and conventional personal computer (PC) based data transfer. Fast response speed is a key criterion if we are to apply OPC methods usefully for *in vivo* applications in thick samples. This is due mainly to the dynamic nature of biological tissue caused by the constant motion of the scatterers within. This rate of change is dependent both on sample thickness and the degree of immobilization. As a reference point, the scattered field of 532 nm light through an unclamped living mouse skin flap has a speckle decorrelation time of ~ 30 ms. When the same tissue is clamped, this decorrelation time increases to ~ 300 ms. [22].

The primary goal of this paper is to show that the use of a high speed DMD (digital mirror device) and FPGA data processing allows DOPC to achieve high response speeds as well. While using the binary modulation of the DMD to accomplish wavefront shaping may seem counter-intuitive and the oblique reflection angle significantly complicates DOPC system alignment, overcoming these challenges enables us to incorporate the strengths of the DOPC while minimizing the response time of the system. In this paper, we report a novel DMD based DOPC system with a demonstrated playback latency of 5.3 ms. We demonstrate our system is capable of focusing light through 2.3 mm thick unclamped mouse dorsal skin with a decorrelation time of less than 30 ms. By repeating the DOPC procedure 50 or even more times per second, we are able to maintain the focus through the living sample indefinitely. This demonstration of sustainable focusing through a thick living sample with blood flowing through it is the first of its kind and opens the door for new applications of OPC in the deep tissue regime of live biological samples.

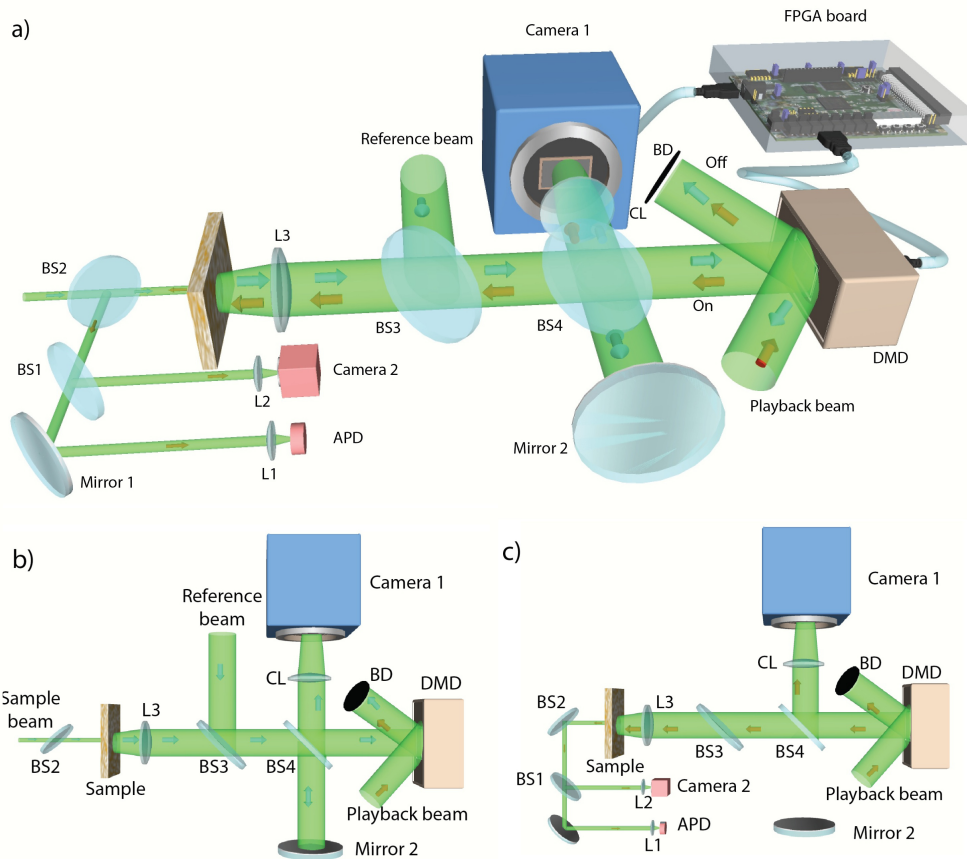


Figure 3.1: (a) Simplified schematic of the DMD based DOPC. A 2.5 mm diameter collimated beam from the laser source (Excelsior 532 nm single mode, 200 mW, Spectra-Physics) is incident onto the sample through BS2. Scattered light from the sample is collected by L3 and is combined with the reference beam by BS3. The combined reference and sample beam is reflected by BS4 and Mirror 2, passes through BS4, and is captured by Camera 1 (pco.edge 5.5, PCO-TECH). The DMD (W4100, Wintech) and Mirror 2 are aligned symmetrically with reference to BS4 and the DMD surface is imaged onto the camera sensor chip by CL (AF-S VR Micro-NIKKOR 105 mm f/2.8G IF-ED, Nikon) with pixel-to-pixel alignment. Camera 1 and the DMD are connected through a host FPGA (ViClaro IV GX Camera Link Development Kit, Microtronix). The conjugate result is observed on Camera 2 (Prosilica GX 1920, Allied Vision) and the APD (SPCM-AQRH-14, Excelitas). (b) Optical path schematic of the recording step. (c) Optical path schematic of the playback step. (L: lens, BS: beamsplitter, BD: beam dump, CL: camera lens, APD: avalanche photo diode).

3.2 Methods

A simplified schematic of the DMD based DOPC system is shown in Fig. 3.1(a). A complete optical scheme can be found in the Supplement. The light paths of the

set-up for recording and playback are shown in Fig. 3.1(b) and (c), respectively. As shown in Fig. 3.1(b), in the recording step, all the pixels on the DMD are turned off. This causes the playback beam to diffract away from Camera 1 and onto a beam dump. The sample beam and reference beams are combined at BS3, reflected by BS4 and Mirror 2, and travel back through BS4 to Camera 1 where their interference pattern is measured. In the playback step shown in Fig. 3.1(c), the FPGA processes the camera data to generate a suitable wavefront solution and sends it to the DMD which displays the corresponding phase map. The playback beam then propagates through BS4, BS3, and L3 to the sample. Meanwhile, the sample beam is blocked by a fast shutter to prevent backscattering off the sample. This playback process results in a focus observed through the sample on Camera 2 and a corresponding peak recorded by the APD. As the reference beam and playback beam are two separate beams, the fluence reflectivity is limited only by the damage threshold of DMD and the laser power. In our system, the fluence reflectivity was set at 2000. As response speed is a design priority, each major component of this system is chosen and adapted for this purpose. We will discuss each component in the following subsections.

Single shot binary phase retrieval

In order to compute the correct phase map to display on the DMD, Camera 1 captures the interference pattern between the reference field $E_{ref}(x, y)$ and the sample field $E_{sam}(x, y)$. This interference pattern can be described as $I_i(x, y) = I_{ref}(x, y) + I_{sam}(x, y) + 2\sqrt{I_{ref}(x, y)I_{sam}(x, y)} \cos |\Delta\theta|$, where $I_{ref}(x, y)$ and $I_{sam}(x, y)$ are the intensity of the reference and sample fields, respectively, and $\Delta\theta$ is their phase difference. By setting $\langle I_{sam}(x, y) \rangle \ll I_{ref}(x, y)$, $I_i(x, y)$ can be approximated as

$$I_i(x, y) \approx I_{ref}(x, y) + 2\sqrt{I_{ref}(x, y)I_{sam}(x, y)} \cos |\Delta\theta| \quad (3.2.1)$$

Then, $I_{ref}(x, y)$ can be measured independently by blocking the sample beam and by comparing it to $I_i(x, y)$, we can determine the range in which the absolute phase difference $|\Delta\theta|$ lies.

$$\begin{aligned} I_i(x, y) < I_{ref} &\rightarrow \frac{\pi}{2} < |\Delta\theta| \leq \pi, \\ I_i(x, y) > I_{ref} &\rightarrow 0 \leq |\Delta\theta| \leq \frac{\pi}{2}. \end{aligned} \quad (3.2.2)$$

In this way, the intensity of the interference pattern at a point (x, y) can be used to recover the binary phase of $E_{sam}(x, y)$ in a single-shot. In comparison, two methods commonly applied in DOPC systems, phase stepping holography [23] and off-axis

holography [24], are capable of fully recovering the sample field but sacrifice either speed or spatial resolution. While DOPC playback with binary phase information is less efficient than with perfect phase information, this small sacrifice in efficiency yields a large enhancement in response speed.

FPGA based data processing and transfer

An FPGA board (as shown in Fig. 3.2) is implemented in the DOPC system for data processing and transfer. It has a Camera Link connection directly to the recording camera and an HDMI (High Definition Multimedia Interface) connection to the DMD. This allows full frame (1920×1080) interference pattern transfer in 5.0 ms (6.8 Gb/s) and full frame size phase map transfer in 1.56 ms (1.8 Gb/s). Here, the phase map transfer time is the time from starting the binary phase data transfer to completing the stable display on the DMD. Although the DMD chip (DLP9500, TI) has a fast refreshing speed of up to 23K fps, the standard 60 Hz HDMI display interface of the W4100 board limits the performance. To fully utilize the fast response speed of the DMD, we designed custom firmware for the FPGA controller (Virtex 5, Xilinx) on the W4100 board. With a custom HDMI protocol, we encode 24 binary pixels into one 24 bit RGB pixel of standard HDMI allowing us to achieve fast binary image transfer. In the recording step, the FPGA board reads out the interference image from the recording camera and retrieves the phase in parallel. Once the phase map is ready and has been adjusted to compensate for the curvature of the DMD (see Supplement), it is transferred to the DMD board and displayed. Compared to a computer, the FPGA allows for greatly accelerated data processing

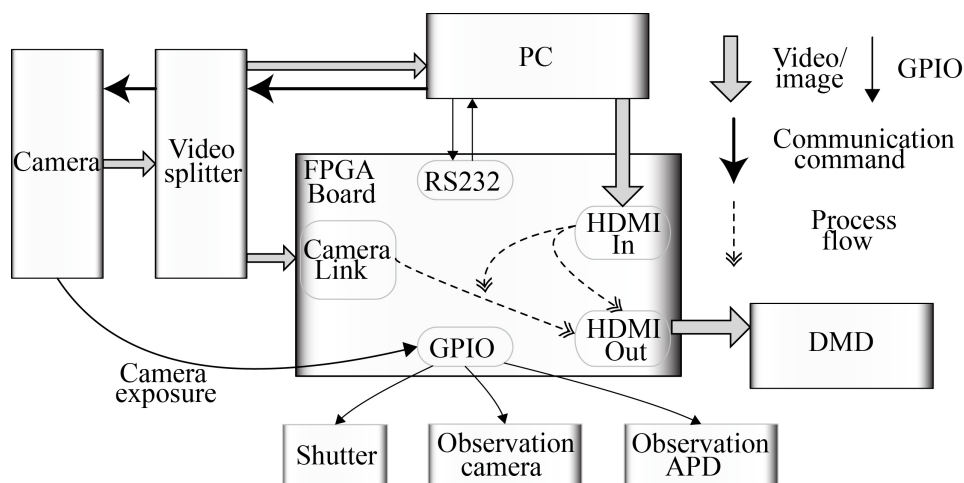


Figure 3.2: Functional schematic of FPGA based DOPC.

and transfer speeds. When using a PC as the host processor in DOPC, the multi-task scheduling and hardware access wrapping in modern operating systems limits the latency between recording and playback steps to a minimum of around two hundred milliseconds [22]. In contrast, as an FPGA inherently has a highly parallel computing capacity, the processing latency for binary phase retrieval is eliminated by overlapping the phase processing with the camera image transfer. In addition to the speed of the FPGA system, our setup allows for data collection and processing to be seamlessly switched to the PC for time-insensitive optical system debugging and pixel-pixel alignment between the recording camera and the DMD. To achieve this, a video splitter (CLV-402, Vivid Engineering) is implemented to switch the output of the recording camera between the PC and the FPGA. An HDMI interface is also set up between the PC and FPGA to allow the PC to transfer phase maps to the DMD.

DMD based phase conjugation

When a conjugate phase map is displayed on the DMD, the DMD implements a binary amplitude modulation scheme [25] to construct a conjugate focus through the tissue. Here we will analyze the binary phase modulation scheme, which although essentially identical to binary amplitude modulation, is formulated here to easily integrate into the framework of phase conjugation [26]. When using the DMD for

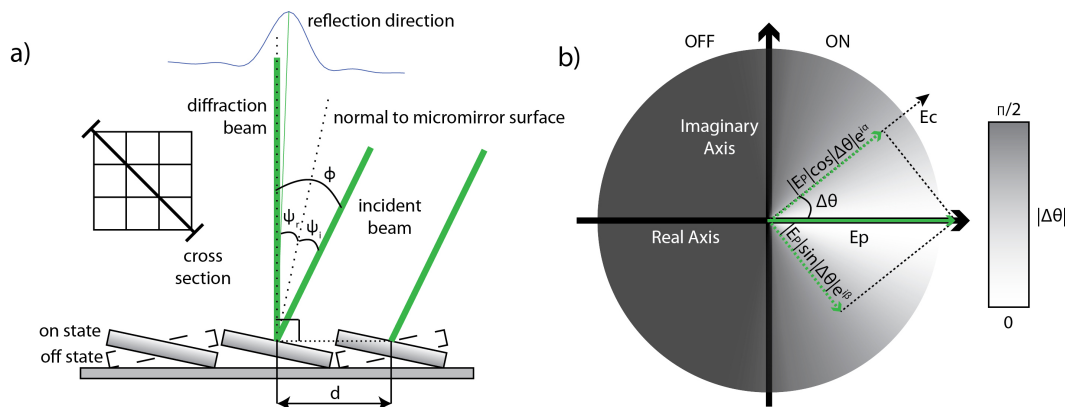


Figure 3.3: (a) DMD diffraction demonstration. (b) Binary phase modulation of DMD. E_p is the field played back by the DMD, E_c is the desired phase conjugate field, and $\Delta\theta$ is the phase difference between E_c and E_p . When a pixel of the DMD is turned on, it plays back the phasor E_p which can be decomposed into two orthogonal components. One is in the direction of the desired phase conjugate field E_c with an amplitude modulated by $\cos |\Delta\theta|$ and contributes to the focus. The other component orthogonal to E_c is modulated by $\sin |\Delta\theta|$ and contributes to the background.

light modulation, every individual micro-mirror acts as a diffractive element and together the whole DMD acts as a 2D blazed grating. As shown in Fig. 3.3(a), when a pixel is turned on, it will tilt 12° clockwise in the diagonal direction. This oblique angle complicates the DOPC system design, as it is a challenge that does not exist for SLM based DOPC systems. To address this, we choose to illuminate the DMD with an appropriately tilted light field such that the diffracted light propagates perpendicularly with respect to the surface of the DMD. This propagation direction is subject to the blazed grating equation, which is a function of the center-to-center distance between the individual micro-mirrors in the array (d), the angle of incidence (ϕ) with respect to the DMD surface normal, the wavelength (λ), and the diffraction order (n). Setting the diffraction angle to fix the diffraction direction normal to the DMD surface yields a simplified form of the blazed grating equation:

$$d \sin \phi = n\lambda. \quad (3.2.3)$$

However, in order to achieve the maximum possible intensity of the diffraction beam, the incident angle should be chosen so that the central peak of the sinc^2 envelope determined by the direction of the specular reflection from each individual micro-mirror matches as closely with the direction normal to the DMD surface as possible. Combining the simplified blazed grating equation above with the law of reflection ($\psi_i = \psi_r$) which determines the location of the sinc^2 envelope, we can solve for the incident angle in order to maximize the intensity of the diffracted beam. Given a light source with a wavelength of 532 nm and $d = 10.8\sqrt{2} \mu\text{m}$ from the dimensions of the DMD, we solve to find the optimum incident angle and diffraction order to be $\phi = 24.7^\circ$ and $n = 12$, respectively.

After optimizing the alignment of the DMD in the DOPC system, we fit the binary amplitude modulation of the DMD into a phase conjugation framework. Since the diffracted light from the DMD has a uniform phase, we can spatially choose whether it is played back or not by manipulating each pixel's state. As shown in Fig. 3.3(b), without loss of generality, we suppose playback beam E_p has uniform amplitude A and phase zero. For an electric field $E_c = |E_c|e^{i\alpha}$ which is the optimal phase conjugate solution to be played back, there is a phase difference $\Delta\theta$ between E_c and E_p . Using the binary phase retrieval algorithm described earlier, we determine whether an individual pixel should be played back. If $|\Delta\theta|$ is less than $\pi/2$, the corresponding pixel is turned on. Otherwise, it is turned off. When we turn on the pixel, E_p can be decomposed into orthogonal phase vectors, as shown in Fig. 3.3(b).

This allows us to derive the phase modulation function of the DMD in DOPC as

$$f(|\Delta\theta|) = \begin{cases} 0, & \frac{\pi}{2} < |\Delta\theta| \leq \pi \\ \cos|\Delta\theta|e^{i\alpha} + \sin|\Delta\theta|e^{i\beta}, & 0 \leq |\Delta\theta| \leq \frac{\pi}{2} \end{cases}. \quad (3.2.4)$$

This means that when $0 \leq |\Delta\theta| \leq \frac{\pi}{2}$ and a pixel of the DMD is turned on to represent a certain E_c , we will play back the electric field $|E_p| \cos|\Delta\theta|e^{i\alpha}$, which has the phase of E_c and amplitude modulated by $\cos|\Delta\theta|$, along with an orthogonal electric field $|E_p| \sin|\Delta\theta|e^{i\beta}$ with amplitude modulated by $\sin|\Delta\theta|$. The cosine term will be played back as a correct component of the phase conjugate field, and construct a peak. The sine term, which has an orthogonal phase, will make no contribution to the peak recovery and will form a background in the playback field. Following a similar derivation in reference [13, 25] (see details in the Supplement), we find the theoretical peak to background ratio (PBR) for DMD based DOPC to be

$$\text{PBR} = \frac{1/2 + (N-1)/2\pi}{M} \approx \frac{N}{2\pi M}, \quad (3.2.5)$$

where M is the number of modes in the focus, and N is the number of controllable modes on DMD. Implementing the DMD in the DOPC setup allows our system to save more than 10 milliseconds for conjugate phase display compared to the time reported in LC-SLM based DOPC systems [13, 15, 22]. When a voltage is applied to an LC-SLM based on nematic liquid crystal technology, it usually takes over 10 milliseconds to turn to the specified direction. This limits the refresh rate to tens of Hz. In contrast, a DMD, which is based on MEMS technology, has a response time around $18 \mu\text{s}$ with a 23 kHz refresh rate [27], over two orders of magnitudes faster than typical LC-SLMs.

Workflow of fast DOPC

The workflow of our system is shown in Fig. 3.4. Prior to operation, the reference beam intensity distribution is recorded. Then the DOPC loop starts. At the beginning of every loop, all the DMD pixels are turned off and the interference pattern is captured. Once the intensity of a pixel is transferred from the camera and stored by the FPGA, its binary phase is processed and recovered. After all the pixels are processed, the binary phase map is transferred to the DMD and displayed for a designated time. During the process, the fast shutter, exposure of the observation camera and the recording of the APD signal are synchronized by the FPGA GPIOs. Each loop is synchronized by the exposure and transfer signals of the recording camera. As shown in Fig. 3.4, the playback latency is the sum of the time required

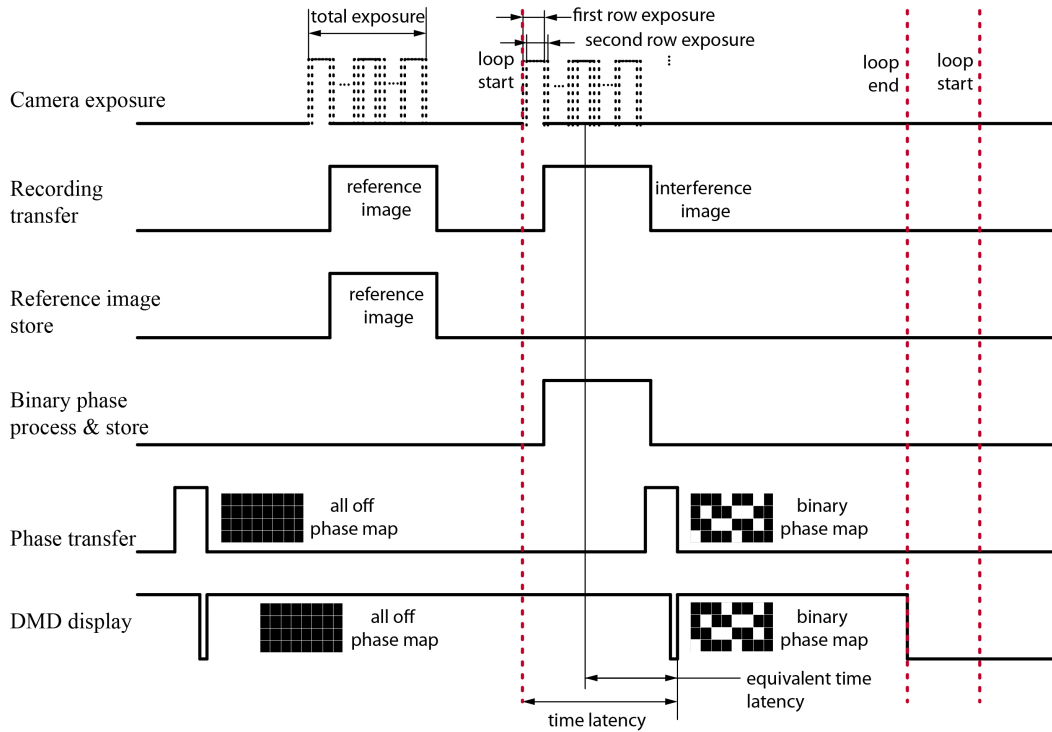


Figure 3.4: Workflow of FPGA based DOPC.

by the recording exposure, data transfer from the recording camera to the FPGA (recording transfer), and binary phase transfer from the FPGA to the DMD (phase transfer). For a full frame size of 1920×1080 (up to 2.1×10^6 controllable modes) and 0.5 ms exposure, the time from the start of the exposure to playback is 7.06 ms. Rolling shutter is used for the recording exposure, so neighbor rows start to expose successively with a $9.17 \mu\text{s}$ delay. The time latency is calculated from the average exposure start time to the time playback starts. The latency is quantified by the following experiments.

3.3 Results

Playback Latency Quantification

To evaluate the actual playback latency of our system, DOPC experiments were conducted on tissue samples with a controllable decorrelation time using a moving tissue strategy [20]. A piece of 3 mm thick chicken breast ($\mu_s = 30/\text{mm}$, $g = 0.965$) was sandwiched between two 1 mm thick glass slides. In the middle layer, a 3 mm thick U shape spacer was placed surrounding the chicken breast to guarantee its thickness and mobility (as shown in Fig. 3.5(a)). During the experiment, samples were changed before they dried out to ensure their scattering properties. The whole

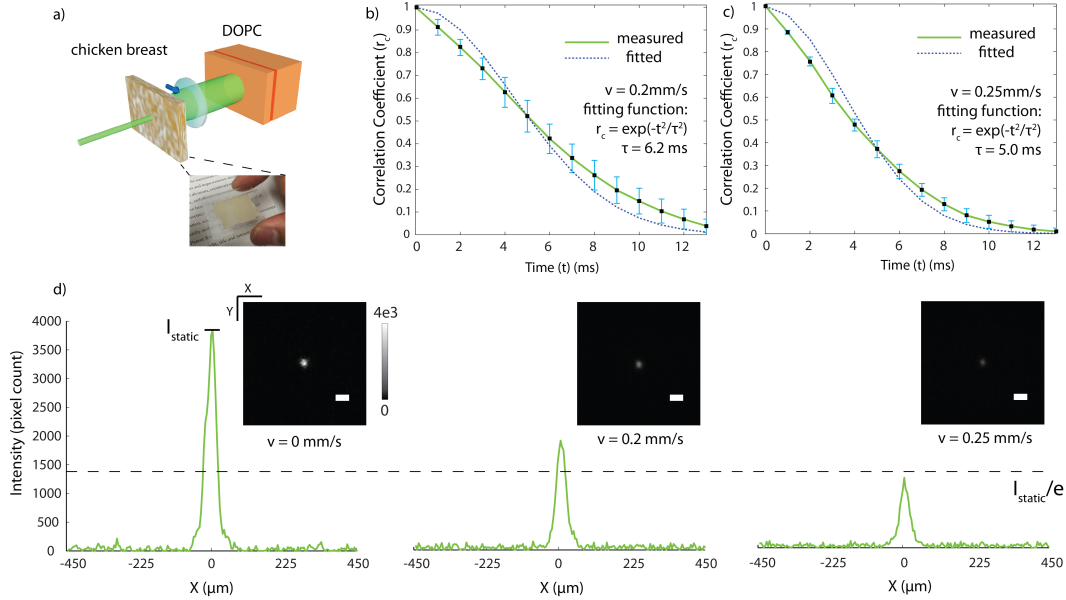


Figure 3.5: (a) Moving sample setup. (b),(c) Moving sample speckle decorrelation curves at lateral velocity 0.2 mm/s and 0.25 mm/s. Error bars indicate standard deviation over 10 datasets. (d) Conjugate focus images and cross section peak plots when the sample was static, moving at 0.2 mm/s and 0.25 mm/s.

sample was held by a translation stage with a motorized actuator (LTA-HS, Newport) to generate different decorrelation times by varying the lateral velocity.

The decorrelation time of the tissue itself was several seconds [13], which was negligible in several milliseconds. To avoid the effects of slow decorrelation when the stage was accelerating, experiments were done when the stage had reached full speed. Tissue decorrelation curves when lateral velocity was set to 0.2 mm/s and 0.25 mm/s are shown in Fig. 3.5(b) and (c), respectively. Here we define the decorrelation time τ as the time t when the speckle correlation coefficient r_c decreases to $1/e$. Fitting with a Gaussian function $r_c = e^{-t^2/\tau^2}$ [28], we can find the decorrelation time τ is 6.2 ms and 5.0 ms for each case. The conjugate focus results for the two cases are shown in Fig. 3.5(d). Given that the motion induced degradation ratio of PBR is identical to the drop in the speckle correlation coefficient [22], it is straightforward to conclude that the system playback latency is identical to the decorrelation time of the sample when the PBR achieved on a moving sample is $1/e$ of the static PBR. From the results, the PBR is 88 for 0.2 mm/s and 56 for 0.25 mm/s. Comparing these to the value of the static PBR divided by e (~ 65), we can tell the time latency is slightly more than 5.0 ms, which can be accurately calculated as 5.3 ms.

OPC Efficiency Quantification

As shown in Eq. 3.2.5, PBR is related to both number of input modes (N , number of speckle grains on DMD) and number of output modes (M , number of speckle grains in the focus). Therefore, it is not a fair comparison to quantify DOPC performance merely by the PBR for different numbers of output modes. However, OPC efficiency, which is ratio of PBR achieved on a system to theoretical PBR, sets a suitable standard for different systems. To evaluate the OPC efficiency of our system, we used our DOPC system to focus light through an opal diffuser (10DIFF-VIS, Newport). Based on the derivation of DMD based conjugation and the measured interference pattern on the recording camera, we determined the speckle size to be 4 pixels wide on the DMD. Since the DMD has 1920×1080 pixels, the number of optical modes we can access with the DMD equals 1.3×10^5 . To determine the number of modes in the focus, we examined the conjugate focus through the sample. When the conjugate beam was played back, we observed a focus on the observation camera with a PBR of 630 and full width half maximum (FWHM) of $45 \mu\text{m}$ as shown in Fig. 3.6. When we displayed a random pattern on the DMD, the speckle FWHM was $13 \mu\text{m}$, computed from the autocorrelation of the speckle pattern. From these two measurements, we can find that the number of modes in the focus is ~ 12 . From the PBR equation, we calculated the optimal PBR as $1.3 \times 10^5 / (12 \cdot 2\pi) \approx 1700$, which means our system performance has an efficiency of 37%.

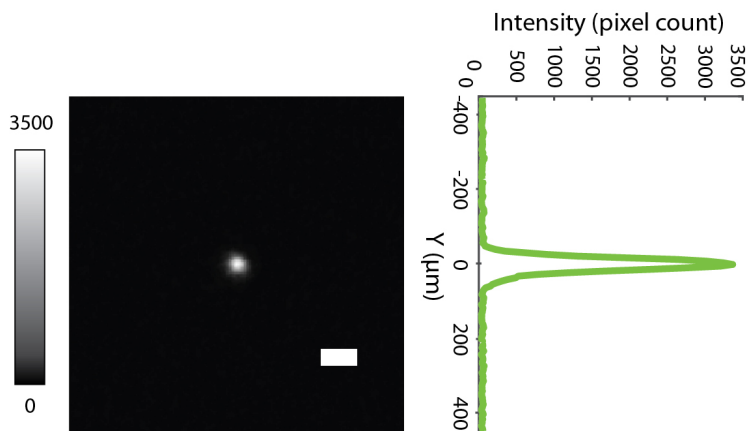


Figure 3.6: PBR quantification. Scale bar is $100 \mu\text{m}$.

***In vivo* Experiments**

In vivo experiments were demonstrated by focusing through the dorsal skin of a living mouse. For the *in vivo* sample, a regular white lab mouse was shaved on the dorsal skin flap. Then its dorsal skin was mounted to a clip device. Isoflurane was implemented as the inhalational anesthesia both in preparation and during the experiment. All of these procedures and the dosage of chemicals followed protocols of the Institutional Animal Care and Use Committee at the California Institute of Technology.

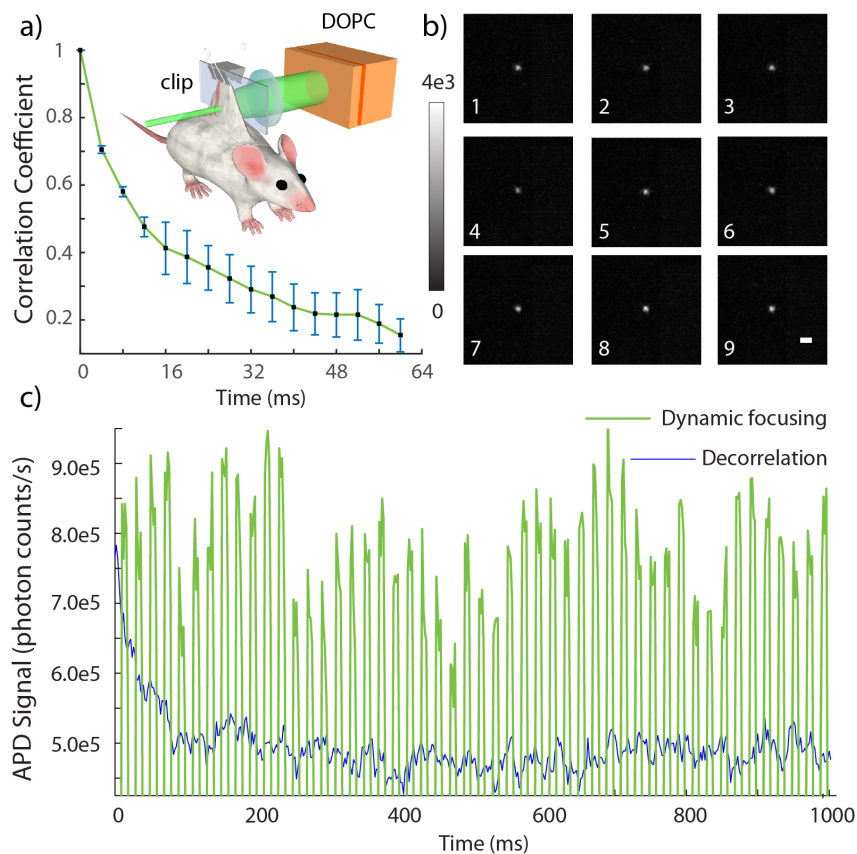


Figure 3.7: (a) Clipped mouse dorsal skin setup and speckle decorrelation curve of *in vivo* tissue. Error bars indicate standard deviation over 10 datasets. (b) Continuous conjugate foci through clipped sample. (c) APD plot for sustainable foci and decorrelation focus. Scale bar is $100\ \mu\text{m}$. In the experiment, to accurately distinguish the focus intensity from background in APD signal a background (I_b) was measured first when the focus totally vanished, which is 5×10^5 in the APD plot.

As shown in Fig. 3.7(a), a clip fixed the upper edge of the skin on a transparent plastic plate, which was placed at the sample position. In this way, the bottom of

the dorsal skin was in a natural free status. The sample beam was incident onto the bottom part of the skin, which had a thickness of around 2.3 mm. Before DOPC was applied, a series of scattering speckle patterns from the tissue were captured by the recording camera to analyze the tissue decorrelation time and form the decorrelation curve plotted in Fig. 3.7(a). From this curve we can tell its decorrelation time is 28 ms, where the decorrelation time is defined as the time when the speckle correlation coefficient decreases to $1/e$. After that, DOPC was conducted with an exposure time of 0.5 ms on the recording camera, at a refresh rate of 50 Hz and a playback holding time of 10 ms. A series of images from the observation camera triggered by the playback signal with an exposure time of 3 ms are included in Fig. Fig. 3.7(b) and Media 1 (5 seconds video) along with a corresponding APD plot in Fig. 3.7(c). From the focus images and APD plot, we can tell a clear focus was constructed and maintained through unrestricted tissue on a living animal. From the average of 10 images we calculate the PBR is 180. For our system, a refresh rate up to 100 Hz with flexible holding time is achievable. It should also be noted that while in the middle of the movie we can observe a short failing of conjugation due to severe body movement from respiration, not due to the decorrelation of the tissue itself.

3.4 Discussion and Conclusion

In this work, we demonstrated the first DMD based DOPC system. This system is capable of playback with latency on the order of milliseconds – a speed improvement of approximately two orders of magnitude over prior DOPC systems. Using the fast DOPC system, we demonstrated the ability to create an indefinitely sustainable focus through unrestricted tissue on a living animal – a capability that has never been previously reported for any OPC experiments. While non-linear approaches can, in principle, provide this capability as well, this DOPC approach is direct and can provide a greater than unity fluence reflectivity. Our system can achieve greater than 2000 fluence reflectivity which is crucial for thick *in vivo* tissue application. In our case, the playback beam is set to ~ 10 mW and the total fluence of the scattered light from the sample is ~ 5 μ W. We further quantified our playback latency as 5.3 ms. While the background due to unmodulated light will need to be addressed in the binary phase retrieval method, it will be straightforward to extend this technology to existing OPC based technology such as TRUE, TROVE, TRACK, etc. and apply it in living tissue for biological applications. Compared to phase only OPC, DMD based DOPC encounters a PBR reduction of 80% (from $\pi/4$ to $1/2\pi$). However, for the DMD based DOPC system the PBR can be further improved by tuning $I_{ref}/\langle I_{sam} \rangle$

in the single-shot binary phase retrieval. For example, suppose I_{ref} and I_{sam} have intensities on the same order of magnitude, then the binary phase retrieval equation will be

$$\text{DMD}(x, y) = \begin{cases} 1, & I_i(x, y) < I_{ref}(x, y) \rightarrow |\alpha - \pi| < \phi \\ \phi = \arccos\left(\frac{1}{2}\sqrt{I_{ref}/I_{sam}}\right) < \frac{\pi}{2} & \\ 0, & \text{else} \end{cases}. \quad (3.4.1)$$

As I_{sam} follows a Rayleigh distribution [29], by comparing the intensity difference we can statistically select a smaller phase range 2ϕ than π . The theoretical PBR in this condition (detailed derivation in the Supplement) is a unimodal function of $I_{ref}/\langle I_{sam} \rangle$, which achieves up to 12.6% higher PBR at $I_{ref}/\langle I_{sam} \rangle = 1.61$ than when $I_{ref} \gg \langle I_{sam} \rangle$. In our experiments, we selected this condition as closely as possible. However, due to the dynamic and heterogeneous nature of biological tissue, it is likely that the PBR could have been further improved by fine tuning this ratio to more accurately select this optimal condition.

Recently, focusing through thin *ex vivo* tissue samples (200 μm chicken breast) was demonstrated at sub-microsecond timescales by using the self-organization of an optical field inside a multimode laser cavity [30]. Despite its speed, the approach demonstrated only around 1000 controllable modes and the number of controllable modes will significantly diminish for thicker samples. This hinders its applications to thick *in vivo* tissue. In addition, the technique relies on optical feedback from the target position, preventing it from being extended to non-invasive techniques with a guide star to focus inside biological tissue.

The flexibility of the DOPC system also provides the additional ability to trade off controllable modes for reduced playback latency. Since the time for recording and phase transfer is proportional to frame size, shrinking the frame size can further decrease the playback latency. For example, if the frame size is reduced to 1920×70 , the playback latency is below 1 ms. Although the PBR will also decrease for smaller frame sizes, up to 1.3×10^5 controllable pixels are still available at a frame size of 1920×70 . In practice, we could balance the number of controllable modes (PBR) and time latency based on the decorrelation properties of different samples.

The architecture of our DOPC system also has the potential to be applied in microsecond scale wavefront shaping. Currently, the playback latency is determined by the sum of the time required by the recording exposure, data transfer from the camera to the FPGA, and binary phase transfer from the FPGA to the DMD. As the

development of fast and sensitive scientific cameras continues, the exposure time and recording transfer time can be reduced by orders of magnitudes. Here we have used an exposure time of 0.5 ms, the minimum exposure time available for the camera, which may be reduced to tens of microseconds or even several microseconds in the future. Meanwhile the sample beam intensity has to match the shorter exposure. This will be hindered by tissue absorption which can be addressed by switching from the 532 nm laser source to near infrared wavelengths, which have orders of magnitude lower tissue absorption. The minimal wavelength dependency of the DOPC system compared to non-linear OPC systems allows this conversion to a different wavelength regime to be direct. We anticipate that with near infrared light, *in vivo* DOPC applications on tissue centimeters thick can be realized. Finally, a phase transfer time around 50 μ s can be realized by using a better FPGA (e.g. Altera Stratix V) and a custom designed data transfer interface to match the maximum refresh rate of the DMD (23 kHz). With the development of faster DMD devices, this time may be further reduced to several microseconds. As the decorrelation rate of tissue drastically increases with thickness, such improvements would ultimately enable wavefront shaping to be applied for optogenetics in the whole brain, *in vivo* deep tissue imaging, and photodynamic therapy for internal organs.

Appendix

Optical Diagram

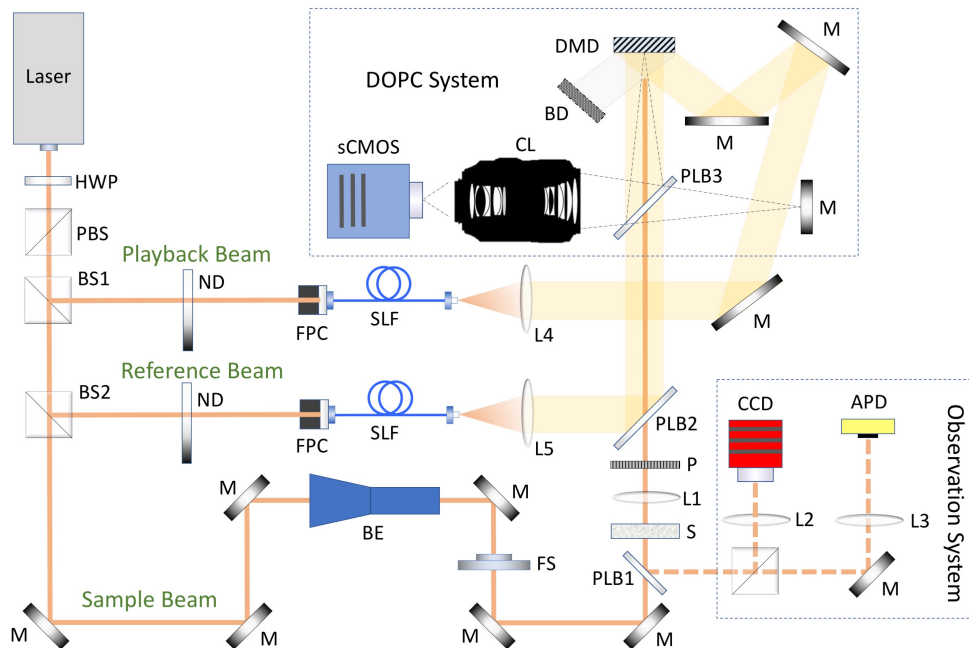


Figure 3.8: Setup diagram. BD: beam dump, BE: beam expander, BS1: 90/10 cube beamsplitter, BS2: 90/10 cube beamsplitter BS3: 50/50 cube beamsplitter, CL: camera lens (Nikon AF-S VR Micro-NIKKOR 105 mm f/2.8G IF-ED), DMD: digital micromirror device (W4100, Wintech), FPC: fiber port connector, HWP: half wave plate, L1: 50 mm planoconvex lens, L2: 100 mm planoconvex lens, L3: 100 mm planoconvex lens, L4: 150 mm planoconvex lens, L5: 15 mm planoconvex lens, M: mirror, ND: neutral density filter, PLB1: 50/50 plate beamsplitter, PLB2: 90/10 plate beamsplitter PLB3: 50/50 plate beamsplitter FS: fast shutter, PBS: polarizing beam splitter, P: polarizer, S: sample, SLF: spatial light filter-single mode polarization maintaining fiber.

DMD Curvature Compensation

The performance of an OPC system is highly dependent on the fidelity between the playback and recording wavefronts. Therefore, curvature of the DMD surface must be taken into account and digitally corrected by finding a compensation phase map for the DMD and adding it to the playback phase map. The compensation phase map is acquired in three steps. First, the playback beam is turned off and the intensity of the reference beam is captured. Second, all the DMD pixels are set to the “on” position, the playback beam is turned on, and the interference pattern between the reference beam and playback beam is captured. Third, the single-shot binary phase

retrieval technique is used to compute the binary wavefront difference between the two beams and find the wavefront distortion due to the curvature of the DMD. In this case, the playback beam is modulated by the curved surface of the DMD and acts as the sample beam in the binary phase retrieval computation. The result of this calculation is a binary phase map which is then applied to each subsequently calculated wavefront in the DOPC procedure before playback.

PBR Derivation

The theoretical performance of optical phase conjugation is well described in framework of Vellekoop [26]. Scattering by tissue essentially maps the input electric field to the output electric field and can be described by a transmission matrix. Assuming the incident electric field on a scattering sample A is E_a and the electric field coming out from the other surface B is E_b , the transformation between E_a and E_b can be described as

$$E_b = T_{AB}E_a, \quad (3.4.2)$$

where T_{AB} is the total transmission matrix describing the propagation of E_a from plane A to B. In perfect phase conjugation, T_{AB} is unitary, which reflects the time symmetry $(T_{AB})^\dagger = (T_{AB})^{-1} = (T_{BA})^*$. If we play back conjugate field E_a^* on plane B, the outcome E'_a on plane A will be,

$$E'_a = T_{BA}E_b^* = T_{BA}(T_{AB}E_a)^* = T_{BA}T_{BA}^{-1}E_a^* = E_a^*, \quad (3.4.3)$$

where “ \dagger ” stands for conjugate transpose. While in practice T_{AB} is only part of the total transmission matrix, we can still derive an approximate phase conjugation solution so that E_a^* is played back on surface A with a background. For a single mode input E_a with unit intensity (without loss of generality), the phase conjugate field in the original position a with background m at plane A will be

$$E'_a = \sum_{b=1}^N t_{ba}E_b^* = \sum_{b=1}^N t_{ba}(t_{ab}E_a)^* = E_a^* \sum_{b=1}^N |t_{ab}|^2 \quad (3.4.4)$$

$$E'_{m,m \neq a} = \sum_{b=1}^N t_{bm}E_b^* = \sum_{b=1}^N t_{bm}(t_{ab}E_a)^* = E_a^* \sum_{b=1}^N t_{bm}t_{ab}^*. \quad (3.4.5)$$

In the case of phase-only modulation with amplitude A , the phase conjugate field is

$$\begin{aligned} E'_a &= A \sum_{b=1}^N t_{ba} e^{i \cdot \arg(E_b^*)} = A \sum_{b=1}^N t_{ab} e^{i \cdot \arg(t_{ab}^* E_a^*)} \\ &= A E_a^* \sum_{b=1}^N |t_{ab}| \end{aligned} \quad (3.4.6)$$

$$E'_{m,m \neq a} = A \sum_{b=1}^N t_{bm} e^{i \cdot \arg(E_b^*)} = A E_a^* \sum_{b=1}^N t_{bm} e^{i \cdot \arg(t_{ab}^*)}. \quad (3.4.7)$$

If a DMD is used as the spatial light modulator in DOPC, the expression for the phase conjugate field at the original position needs to be modified to account for the binary modulation of the DMD. This can be written as

$$E'_a = \sum_{b=1}^N t_{ba} A f(|\Delta\theta|), \quad (3.4.8)$$

where $|\Delta\theta| = |\alpha - \theta_p|$, $\alpha = \arg(E_b^*)$, θ_p is the phase of playback light from the DMD, and $f(|\Delta\theta|)$ is the phase modulation function of the DMD given by

$$f(|\Delta\theta|) = \begin{cases} 0, & |\Delta\theta| > \phi \\ \cos |\Delta\theta| e^{i\alpha} + \sin |\Delta\theta| e^{i\beta}, & |\Delta\theta| \leq \phi \end{cases}, \quad (3.4.9)$$

where β is the argument of the decomposed phasor orthogonal to $e^{i\alpha}$. Pixels with an absolute phase difference less than or equal to the upper bound ϕ are turned on for playback. With phase stepping or off-axis holography, we can easily select any ϕ . When $0 \leq |\Delta\theta| < \phi$, we can decompose E'_a into two terms. The first term is a phase only conjugation term modulated by $\cos |\Delta\theta|$. As the phase distribution of speckles is uniform within the selected range, the second term, which has an orthogonal phase, will make no contribution to recovery of the peak. From the above, we can intuitively come to the result that DMD based DOPC is phase only DOPC with an amplitude modulated by the cosine term, as shown in Eq. 3.4.10 below.

$$\begin{aligned} E'_a &= \sum_{b=1}^N t_{ba} A f(|\Delta\theta|) \\ &= \sum_{b=1}^N t_{ba} A e^{i \cdot \arg(E_b^*)} \cos |\Delta\theta| (|\Delta\theta| \leq \phi) \\ &= \sum_{b=1}^N t_{ba} A e^{i \cdot \arg(t_{ab}^* E_a^*)} \cos |\Delta\theta| (|\Delta\theta| \leq \phi) \\ &= A E_a^* \sum_{b=1}^N |t_{ab}| \cos |\Delta\theta| (|\Delta\theta| \leq \phi). \end{aligned} \quad (3.4.10)$$

Since the transmission matrix elements can be assumed to follow complex circular Gaussian distribution [26], the amplitudes of the individual matrix elements $|t_{ab}|$ follow a Rayleigh distribution $|t_{ab}| : \text{Rayleigh}(\sigma)$ and their intensities $|t_{ab}|^2$ follow an exponential distribution $|t_{ab}|^2 \sim e^{-1/(2\sigma^2)}$ with $2\sigma^2$ as the ensemble average intensity of each element. The absolute phase difference $|\Delta\theta|$ follows a uniform distribution from 0 to π . Then, based on the derivation of phase-only phase conjugation described by Wang [13], the peak intensity and its ensemble average are calculated as

$$\begin{aligned}
I'_a &= \left| A \sum_{b=1}^N |t_{ab}| \cos |\Delta\theta| (|\Delta\theta| \leq \phi) \right|^2 \\
&= A^2 \sum_{b=1}^N |t_{ab}|^2 (\cos |\Delta\theta| (|\Delta\theta| \leq \phi))^2 \\
&+ A^2 \left\{ \sum_{b=1}^N \sum_{b' \neq b}^N |t_{ab}| |t_{ab'}| (\cos |\Delta\theta| (|\Delta\theta| \leq \phi))^2 \right\}^2. \tag{3.4.11}
\end{aligned}$$

$$\begin{aligned}
\langle I'_a \rangle &= A^2 N \langle |t_{ab}|^2 \rangle \langle (\cos |\Delta\theta| (|\Delta\theta| \leq \phi))^2 \rangle \\
&+ A^2 N(N-1) \langle |t_{ab}|^2 \rangle \langle \cos (|\Delta\theta|) (|\Delta\theta| \leq \phi) \rangle^2 \\
&= 2NA^2\sigma^2 \left(\frac{\sin 2\phi/2 + \phi}{2\pi} \right) \\
&+ \frac{\pi}{2} N(N-1) A^2 \sigma^2 \left(\frac{\sin \phi}{\pi} \right)^2 \tag{3.4.12}
\end{aligned}$$

Similarly, the background can be calculated as

$$E'_{m,m \neq a} = \sum_{b=1}^N t_{bm} A e^{i\theta_p} (|\Delta\theta| \leq \phi) \tag{3.4.13}$$

$$I'_{m,m \neq a} = A^2 \left| \sum_{b=1}^N t_{bm} (|\Delta\theta| \leq \phi) \right|^2 \tag{3.4.14}$$

$$\begin{aligned}
\langle I'_{m,m \neq a} \rangle &= A^2 \left\langle \left| \sum_{b=1}^N t_{bm} (|\Delta\theta| \leq \phi) \right|^2 \right\rangle \\
&= 2NA^2\sigma^2 \frac{\phi}{\pi}. \tag{3.4.15}
\end{aligned}$$

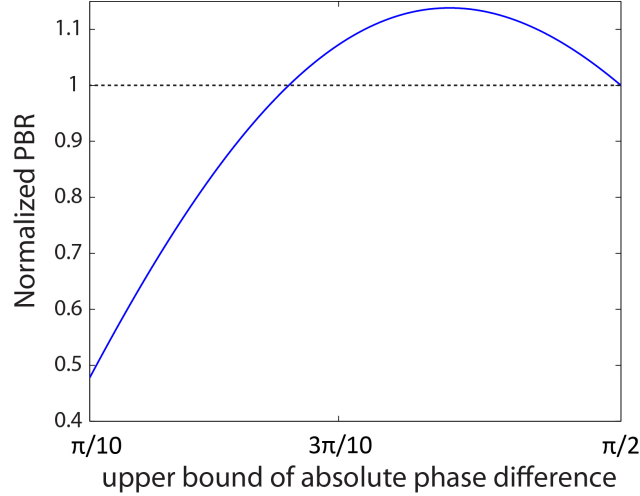


Figure 3.9: Normalized theoretical PBR with respect to ϕ (the upper bound of the absolute phase difference).

Putting these two expressions together, we can find the PBR to be

$$\begin{aligned}
 \text{PBR}_{\text{DMD}} &= \frac{\langle I'_a \rangle}{\langle I'_{m,m \neq a} \rangle} \\
 &= \frac{2NA^2\sigma^2 \left(\frac{\sin 2\phi/2 + \phi}{2\pi} \right) + \frac{\pi}{2}N(N-1)A^2\sigma^2 \left(\frac{\sin \phi}{\pi} \right)^2}{2NA^2\sigma^2 \frac{\phi}{\pi}} \\
 &= \frac{1}{2} + \frac{\sin 2\phi + (N-1)\sin^2 \phi}{4\phi} \\
 &\approx \frac{N \sin^2 \phi}{4\phi}. \tag{3.4.16}
 \end{aligned}$$

For $\phi = \pi/2$, the PBR is

$$\text{PBR}_{\text{DMD}, \phi = \pi/2} = \frac{1}{2} + \frac{(N-1)}{2\pi} \approx \frac{N}{2\pi}, \tag{3.4.17}$$

which is consistent with derivation in iterative binary iterative wavefront optimization [25]. As shown in Fig. 3.9, the PBR is a unimodal function of ϕ , reaching its maximum at $\phi = 0.371\pi$, with a 13.8% higher value than at $\phi = \pi/2$. When there are M nonzero optical modes in focus, the PBR is scaled by M so that the new PBR is

$$\text{PBR}_{\text{DMD}} \approx \frac{N \sin^2 \phi}{4M\phi}. \tag{3.4.18}$$

Single-shot Binary Phase Retrieval

Using a reference beam with an electric field $E_{ref}(x, y)$ (whose intensity is $I_{ref}(x, y)$ and phase is zero without loss generality), the complex information (phase and amplitude) of the sample field $E_{sam}(x, y)$ (whose intensity is $I_{sam}(x, y)$ and phase is α) is coupled into the intensity of their interference pattern I_i as

$$I_i(x, y) = I_{ref}(x, y) + I_{sam}(x, y) + 2\sqrt{I_{ref}(x, y)I_{sam}(x, y)} \cos \alpha. \quad (3.4.19)$$

For phase retrieval in DMD based DOPC, only the condition $\frac{\pi}{2} < \alpha < \frac{3\pi}{2}$ or $-\frac{\pi}{2} \leq \alpha \leq \frac{\pi}{2}$ is needed. This allows a single-shot binary phase retrieval technique to be used to determine which DMD pixels should be turned on.

$$\text{DMD}(x, y) = \begin{cases} 1, & I_i(x, y) < I_{ref}(x, y) \rightarrow B(\alpha) = \pi \\ 0, & \text{else} \rightarrow B(\alpha) = 0 \end{cases}. \quad (3.4.20)$$

It can be shown that $I_i(x, y) < I_{ref}(x, y) \rightarrow \frac{\pi}{2} < \alpha < \frac{3\pi}{2}$. For this phase range of interest, the absolute phase difference is defined as $|\Delta\theta| = |\alpha - \pi|$. To derive the PBR, new notations are defined $r = I_{sam}/4I_{ref}$ and $g = I_{ref}/\langle I_{sam} \rangle$. For a pixel with specific phase α , its status is controlled by the intensity ratio of the reference and sample signal as derived from Eqs. 3.4.19 and 3.4.20,

$$\text{DMD}(x, y) = \begin{cases} 1, & \cos |\Delta\theta| > \sqrt{r} \\ 0, & \text{else} \end{cases}. \quad (3.4.21)$$

As the absolute phase distribution of $\frac{\pi}{2} < \alpha < \frac{3\pi}{2}$ is uniform within $(0, \frac{\pi}{2})$, given an intensity I_{sam} , the upper phase difference bound of “on” pixels is

$$\phi = \begin{cases} \arccos(\sqrt{r}) & r \leq 1 \\ 0, & \text{else} \end{cases}. \quad (3.4.22)$$

Since the sample intensity follows a Rayleigh distribution $I_{sam} : \text{Rayleigh}(\sigma)$, the ratio r also follows a Rayleigh distribution with a scale parameter given by

$$\sigma_r = \sigma_{I_{sam}}/4I_{ref} = \frac{\sigma_{I_{sam}}}{4g\langle I_{sam} \rangle} = \frac{\sigma}{2\sqrt{2\pi}g\sigma} = \frac{1}{2\sqrt{2\pi}g}. \quad (3.4.23)$$

The peak intensity can then be derived from Eq. 3.4.12:

$$\begin{aligned}
\langle I_{peak} \rangle &\approx \frac{\pi}{2} N(N-1) A^2 \sigma^2 \left\langle \left(\frac{\sin \phi}{\pi} \right)^2 \right\rangle \\
&= \frac{\pi}{2} N(N-1) A^2 \sigma^2 \left(\int_0^1 \frac{1-r}{\pi^2} f(r) dr + \int_1^\infty \frac{0}{\pi^2} f(r) dr \right) \\
&= \frac{1}{2\pi} N(N-1) A^2 \sigma^2 \int_0^1 (1-r) \frac{r}{\sigma_r^2} e^{-r^2/(2\sigma_r^2)} dr \\
&= \frac{1}{2\pi} N(N-1) A^2 \sigma^2 \left[1 - \sqrt{\frac{\pi}{2}} \sigma_r^2 (1 - e^{-1/\sigma_r^2}) \right] \\
&= \frac{1}{2\pi} N(N-1) A^2 \sigma^2 \left[1 - \sqrt{\frac{1 - e^{-8\pi g^2}}{16g^2}} \right]. \tag{3.4.24}
\end{aligned}$$

In the same way, the background can be derived from Eq. 3.4.15:

$$\begin{aligned}
\langle I_{background} \rangle &= \frac{2NA^2\sigma^2}{\pi} \langle \phi \rangle \\
&= \frac{2NA^2\sigma^2}{\pi} \left(\int_0^1 \arccos(\sqrt{r}) f(r) dr + \int_1^\infty 0 f(r) dr \right) \\
&= \frac{2NA^2\sigma^2}{\pi} \int_0^1 \arccos(\sqrt{r}) \frac{r}{\sigma_r^2} e^{-r^2/(2\sigma_r^2)} dr \\
&= 16Ng^2NA^2\sigma^2 \int_0^1 \arccos(\sqrt{r}) r e^{-4\pi g^2 r^2} dr. \tag{3.4.25}
\end{aligned}$$

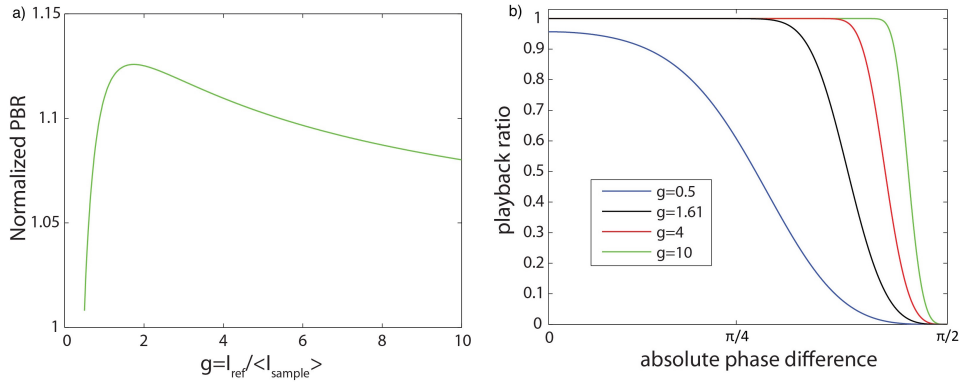


Figure 3.10: **Single shot binary phase retrieval:** (a) The normalized theoretical PBR (relative to $\text{PBR}_{\text{DMD}, \phi = \pi/2}$) with respect to the intensity ratio g of the reference and sample beam. (b) The playback ratio function for different intensity ratios g .

So, calculating the PBR from these two quantities gives

$$\begin{aligned}
\text{PBR}_{\text{DMD},g = I_{ref}/\langle I_{sam} \rangle} &= \frac{\langle I_{peak} \rangle}{\langle I_{background} \rangle} \\
&= \frac{\frac{1}{2\pi} N (N - 1) A^2 \sigma^2 \left[1 - \sqrt{\frac{1 - e^{-8\pi g^2}}{16g^2}} \right]}{16Ng^2 NA^2 \sigma^2 \int_0^1 \arccos(\sqrt{r}) r e^{-4\pi g^2 r^2} dr} \\
&= \frac{(N - 1) \left[1 - \sqrt{\frac{1 - e^{-8\pi g^2}}{16g^2}} \right]}{32\pi g^2 \int_0^1 \arccos(\sqrt{r}) r e^{-4\pi g^2 r^2} dr} \\
&\approx \frac{N \left[1 - \sqrt{\frac{1 - e^{-8\pi g^2}}{16g^2}} \right]}{32\pi g^2 \int_0^1 \arccos(\sqrt{r}) r e^{-4\pi g^2 r^2} dr}, \tag{3.4.26}
\end{aligned}$$

which is a unimodal function of the intensity ratio g . For $\langle I_{sam} \rangle \ll I_{ref}$, $g \rightarrow \infty$ and the PBR is $\text{PBR}_{\text{DMD},\phi = \pi/2}$. As shown in Fig. 3.10(a), the function reaches its maximum at $g = 1.61$, having a value 12.6% higher than $\text{PBR}_{\text{DMD},\phi = \pi/2}$. This is consistent with Eq. 3.4.16, where the maximum value position is at $\phi = 0.371\pi$ equal to $\arccos(1/(2\sqrt{g}))$. The inherent statistical phase selection capacity of single-shot phase modulation allows us to achieve a PBR enhancement nearly equivalent to that offered by selecting the optimal bound ϕ from the exact phase map. According to Eq. 3.4.21, given a pixel with absolute phase difference $|\Delta\theta| < \pi/2$ and intensity I_{sam} , it will be turned on for playback when

$$\phi = \arccos(\sqrt{r}) = \arccos\left(\sqrt{I_{sam}/4I_{ref}}\right) > |\Delta\theta|. \tag{3.4.27}$$

For all pixels with an absolute phase difference $|\Delta\theta|$, as $r = I_{sam}/4I_{ref}$ follows a Rayleigh distribution, the fraction of pixels on will be

$$\begin{aligned}
p_{on}(|\Delta\theta|) &= \int_{|\Delta\theta|}^{\pi/2} f(\phi) d\phi \\
&= \int_0^{\cos^2|\Delta\theta|} \frac{r}{\sigma_r^2} e^{-r^2/(2\sigma_r^2)} dr \\
&= 1 - e^{-4\pi g^2 \cos^4|\Delta\theta|}. \tag{3.4.28}
\end{aligned}$$

The playback ratio function is plotted for different intensity ratios in Fig. 3.10(b).

References

- [1] Ivo M Vellekoop and Allard P Mosk. “Focusing coherent light through opaque strongly scattering media”. In: *Optics Letters* 32.16 (2007), pp. 2309–2311.
- [2] Allard P Mosk et al. “Controlling waves in space and time for imaging and focusing in complex media”. In: *Nature photonics* 6.5 (2012), pp. 283–292.
- [3] Ivo M Vellekoop, Ad Lagendijk, and Allard P Mosk. “Exploiting disorder for perfect focusing”. In: *Nature Photonics* 4.5 (2010), pp. 320–322.
- [4] Donald B Conkey, Antonio M Caravaca-Aguirre, and Rafael Piestun. “High-speed focusing of light through dynamic turbid media”. In: *Computational Optical Sensing and Imaging*. Optical Society of America. 2012, CTu4B–6.
- [5] Hasan Yilmaz, Willem L Vos, and Allard P Mosk. “Optimal control of light propagation through multiple-scattering media in the presence of noise”. In: *Biomedical optics express* 4.9 (2013), pp. 1759–1768.
- [6] SM Popoff et al. “Image transmission through an opaque material”. In: *arXiv preprint arXiv:1005.0532* (2010).
- [7] Thomas Chaigne et al. “Controlling light in scattering media non-invasively using the photoacoustic transmission matrix”. In: *Nature Photonics* 8.1 (2014), pp. 58–64.
- [8] Jonghee Yoon et al. “Measuring optical transmission matrices by wavefront shaping”. In: *Optics Express* 23.8 (2015), pp. 10158–10167.
- [9] Zahid Yaqoob et al. “Optical phase conjugation for turbidity suppression in biological samples”. In: *Nature photonics* 2.2 (2008), pp. 110–115.
- [10] Chia-Lung Hsieh et al. “Digital phase conjugation of second harmonic radiation emitted by nanoparticles in turbid media”. In: *Optics express* 18.12 (2010), pp. 12283–12290.
- [11] Haowen Ruan et al. “Iterative time-reversed ultrasonically encoded light focusing in backscattering mode”. In: *Scientific reports* 4 (2014), p. 7156.
- [12] Xiao Xu, Honglin Liu, and Lihong V Wang. “Time-reversed ultrasonically encoded optical focusing into scattering media”. In: *Nature photonics* 5.3 (2011), pp. 154–157.
- [13] Ying Min Wang et al. “Deep-tissue focal fluorescence imaging with digitally time-reversed ultrasound-encoded light”. In: *Nature communications* 3 (2012), p. 928.
- [14] Benjamin Judkewitz et al. “Speckle-scale focusing in the diffusive regime with time reversal of variance-encoded light (TROVE)”. In: *Nature photonics* 7.4 (2013), pp. 300–305.

- [15] Edward Haojiang Zhou et al. “Focusing on moving targets through scattering samples”. In: *Optica* 1.4 (2014), pp. 227–232.
- [16] Cheng Ma et al. “Time-reversed adapted-perturbation (TRAP) optical focusing onto dynamic objects inside scattering media”. In: *Nature photonics* 8.12 (2014), pp. 931–936.
- [17] Puxiang Lai et al. “Time-reversed ultrasonically encoded optical focusing in biological tissue”. In: *Journal of Biomedical Optics* 17.3 (2012), pp. 0305061–0305063.
- [18] Puxiang Lai et al. “Focused fluorescence excitation with time-reversed ultrasonically encoded light and imaging in thick scattering media”. In: *Laser Physics Letters* 10.7 (2013), pp. 075604–075609.
- [19] Cheng Ma, Xiao Xu, and Lihong V Wang. “Analog time-reversed ultrasonically encoded light focusing inside scattering media with a 33,000× optical power gain”. In: *Scientific Reports* 5 (2015).
- [20] Yan Liu et al. “Optical focusing deep inside dynamic scattering media with near-infrared time-reversed ultrasonically encoded (TRUE) light”. In: *Nature Communications* 6 (2015).
- [21] B Jayet, J-P Huignard, and F Ramaz. “Optical phase conjugation in Nd:YVO 4 for acousto-optic detection in scattering media”. In: *Optics Letters* 38.8 (2013), pp. 1256–1258.
- [22] Mooseok Jang et al. “Relation between speckle decorrelation and optical phase conjugation (OPC)-based turbidity suppression through dynamic scattering media: a study on in vivo mouse skin”. In: *Biomedical optics express* 6.1 (2015), pp. 72–85.
- [23] Ichirou Yamaguchi and Tong Zhang. “Phase-shifting digital holography”. In: *Optics Letters* 22.16 (1997), pp. 1268–1270.
- [24] Michael Liebling, Thierry Blu, and Michael Unser. “Complex-wave retrieval from a single off-axis hologram”. In: *Journal of the Optical Society of America A* 21.3 (2004), pp. 367–377.
- [25] Duygu Akbulut et al. “Focusing light through random photonic media by binary amplitude modulation”. In: *Optics Express* 19.5 (2011), pp. 4017–4029.
- [26] Ivo Micha Vellekoop. “Controlling the propagation of light in disordered scattering media”. In: *arXiv preprint arXiv:0807.1087* (2008).
- [27] Dana Dudley, Walter M Duncan, and John Slaughter. “Emerging digital micromirror device (DMD) applications”. In: *Micromachining and Microfabrication*. International Society for Optics and Photonics. 2003, pp. 14–25.

- [28] Giorgio Volpe, Giovanni Volpe, and Sylvain Gigan. “Brownian motion in a speckle light field: tunable anomalous diffusion and selective optical manipulation”. In: *Scientific Reports* 4 (2014).
- [29] Joseph W Goodman. *Statistical Optics*. Vol. 1. Wiley-Interscience, 2000.
- [30] Micha Nixon et al. “Real-time wavefront shaping through scattering media by all-optical feedback”. In: *Nature Photonics* 7.11 (2013), pp. 919–924.